RSC Advances

PAPER

View Article Online
View Journal | View Issue

Cite this: *RSC Adv.*, 2019, **9**, 15715

Nitrogen, sulfur-codoped micro–mesoporous carbon derived from boat-fruited sterculia seed for robust lithium–sulfur batteries†

Jian Wu,‡[a] Qi Zhang,‡[a] Mo Li,[a] Jian Yan,[bc] Yong Zhang,[bc] Jiaqin Liu*[ac] and Yucheng Wu[bc]

The diverse textures and tunable surface properties of abundant bioresources offer great opportunities to utilize biochar materials as sulfur hosts for naturally boosting the electrochemical performances of Li–S batteries. Herein, a N, S-codoped micro–mesoporous carbon was synthesized from boat-fruited sterculia seed, and used as a sulfur host matrix for Li–S batteries. After sulfur infiltration (≈62% sulfur) and cell assembly, the obtained S/NSBC cathode shows outstanding discharge–charge performance, good rate capability, and especially long cycling stability. A high initial discharge capacity of 1478 mA h g^{-1} was achieved at 0.1C, and the reversible discharge capacity was still retained at 649 mA h g^{-1} after 500 cycles at 0.5C with ultralow decay rate of 0.08% per cycle, and especially zero-capacity-decay after 300 cycles. Such superior electrochemical performance of S/NSBC cathode is attributed to the synergy of the unique 3D conductive micro–mesoporous frameworks and huge N, S-codoped polar surface within the carbon matrix, which can physically confine the dissolved polysulfides within the pore structures, and chemically anchor the polysulfides through chemical interaction between lithium polysulfides and N and S sites, thus enabling the favorable reaction kinetics, efficient utilization of sulfur, and effective mitigation of polysulfide diffusion and shuttling within the cathode. This work well manifests the great feasibility and superiority of utilizing bioresources for high performance Li–S batteries.

Received 19th March 2019
Accepted 2nd May 2019

DOI: 10.1039/c9ra02037c

rsc.li/rsc-advances

Introduction

Lithium–sulfur (Li–S) batteries have recently attracted great interest as a promising electrochemical device for energy conversion and storage applications because of their high theoretical specific capacity (1675 mA h g^{-1}) and energy density (~2500 W h kg^{-1}), low-cost, and environmental friendliness. Despite these advantages, the practical applications of Li–S batteries is still impeded by several critical obstacles, including the insulating nature of sulfur and its end-discharge products (Li_2S_2/Li_2S), large volumetric expansion/shrinkage (80%) during discharge/charge process, and most seriously, severe polysulfides (Li_2S_n, $4 \leq n \leq 8$) shuttling between cathode and anode (shuttling effect), thereby leading to the low sulfur utilization, short cycle life, anode corrosion, and poor mechanical integrity of the electrodes.[1–4] Many strategies have been developed to address these problems, including the design of novel cathode materials, electrolytes, anode protections, and battery structures.[5–9]

Incorporating sulfur into conductive host matrix, typically porous carbon materials, is especially promising, because porous carbon frameworks could not only effectively improve the electrical conductivity of sulfur cathode, but also physically confine the dissolved polysulfides within the cathode during cycling.[10–13] Various porous carbon materials, such as ordered mesoporous carbon,[14–16] carbon aerogels,[17,18] carbon nanotubes,[19–21] and a variety of porous carbon composites,[22–24] have already been employed as sulfur hosts to trap polysulfides within pores while guaranteeing the electron pathway. Nonetheless, migration of polysulfides is hard to be completely prevented by physical confinement of polysulfides within the voids of porous carbon materials. Surface modification of the carbon hosts by heteroatom doping has already been demonstrated to effectively suppress the polysulfides shuttling because of the chemical interaction between the polar lithium polysulfides and hetero-doped sites on carbon surface.[25–28] Various single- or dual-heteroatom doping to tune the surface properties of carbon host matrix have been extensively applied to boost the electrochemical performance of Li–S batteries. Wang's group[29] reported the functional groups of N-doped carbon composite

[a]*Institute of Industry and Equipment Technology, Hefei University of Technology, Hefei 230009, China. E-mail: jqliu@hfut.edu.cn*

[b]*School of Materials Science and Engineering, Hefei University of Technology, Hefei, 230009, China*

[c]*Key Laboratory of Advanced Functional Materials and Devices of Anhui Province, Hefei 230009, China*

† Electronic supplementary information (ESI) available. See DOI: 10.1039/c9ra02037c

‡ Jian Wu and Qi Zhang contributed equally.

enabled the strong chemisorption of lithium polysulfides on electroactive sites within the cathode, leading to a greatly improved electrochemical performance. Manthiram's group[30] adopted the porous N, S-codoped graphene sponge as a 3D conductive scaffold to accommodate the dissolved lithium polysulfides and obtain the Li/polysulfides batteries electrodes. Compared with the rGO, S-doped and N-doped graphene electrodes, the N, S-codoped graphene electrode realized higher energy density and longer cyclic life, which could be attributed to the chemical binding of lithium polysulfides to N and S sites in graphene, suppressing the sulfur loss during the discharge/charge process.

Biomass-derived biochar materials have been recently investigated as sulfur hosts for Li–S batteries thanks to their low-cost, resource abundance, simple preparation, and environment friendliness. Various biochar materials derived from pomelo peel,[31] litchi shell,[32] cherry pit,[33] corncob,[34] coconut shell,[35] mushroom,[36] silk cocoon,[37] rice husk,[38] gelatin,[39] *etc.* have been synthesized by carbonizing the natural frameworks of biomass, and successfully applied in Li–S batteries as the conductive sulfur host matrix. The textural and compositional characteristics of biomass have significant impact on the morphologies, microstructures and surface properties of the prepared biochar.[35,40] Diverse biomass precursors combined with different preparation processes may derive out different types of biochar with particular microstructures and surface properties, thus offering great opportunities to develop and utilize biochar materials in rechargeable Li–S battery.

Boat-fruited sterculia seed (BSS) is a tropical herb of the Sterculiaceae family, mainly distributed in Indonesia, Malaysia, Vietnam, as well as Southeast China, and commonly used in traditional Chinese medicine to treat many diseases,[41] such as hoarseness of voice, sore throat, and *etc.* It is worth noting that the BSS has a quite high water-absorbing capacity, similar to the "compressed sponge", bringing about striking volume expansion after water-absorption (Fig. S1†) due to its inherent texture. This characteristic may enable the BSS-derived carbon with peculiar microstructures to be an ideal potential sulfur host. Herein, we developed a micro–mesoporous N–S codoped BSS-derived carbon (NSBC) by a two-step procedure of carbonization–activation combined with N, S-codoping. After loading sulfur into the pores of NSBC (~62% sulfur content), the S/NSBC cathode presented outstanding discharge–charge performance, high rate capability, and long cycling stability, with an initial discharge capacity of 1478 mA h g^{-1} at 0.1C, an average capacity decay as low as 0.08% per cycle for 500 cycles, and especially zero-capacity-decay after 300 cycles at 0.5C. To the best of our knowledge, such superior electrochemical performance and high cycling stability have rarely been reported with regarding to the biochar-based sulfur cathodes.

Experimental section

Synthesis of BC

The BSS used in this work was produced in Guangdong province of China. After removing the kernel, the BSS powder was put into a Teflon-lined autoclave and maintained at 180 °C for 6 h by hydrothermal treatment. The resulting brownish black precipitate was filtered, washed, and dried at 60 °C. Afterwards, the obtained precursor was mixed with 5 M potassium hydroxide–ethanol solution for 18 h under vigorous stirring with 3 : 1 mass ratio of precursor to KOH, then the dried mixture was simultaneously carbonized and activated at 800 °C for 2 h at a heating rate of 5 °C min^{-1} under argon. Finally, the obtained black precipitate was washed with 1 M HCl and deionized water, and dried overnight at 60 °C to obtain the BSS-derived carbon (denoted as BC).

Preparation of NSBC

A slurry was obtained by mixing BC with 50 mg ml^{-1} thiourea solution with carbon to thiourea mass ratio of 1 : 4 under vigorous stirring at 80 °C. Then, the slurry was heat-treated at 800 °C for 3 h under argon at a heating rate 5 °C min^{-1}. The resulting product was washed with 1 M HCl and deionized water successively, and dried overnight at 60 °C to obtain the N, S-codoped BSS-derived carbon (denoted as NSBC).

Fabrication of S/NSBC cathode

The S-infiltrated NSBC composite (denoted as S/NSBC) was fabricated using a melt-diffusion strategy by mixing sulfur with NSBC in a weight ratio of 65 : 35. Then, the hybrid was ground and heat-treated in a steel container at 155 °C for 12 h. The cathode slurry was obtained by ball milling 80 wt% S/NSBC, 10 wt% Super P and 10 wt% poly(vinylidene fluoride) binder in *N*-methyl-2-pyrrolidone solvent. The uniform slurry was casted onto an aluminum foil substrate, dried at 60 °C overnight, and punched into pieces with a diameter of 12 mm and an average areal sulfur mass of 1.3–1.5 mg cm^{-2}. For comparison, the S/BC composite was also fabricated following the same procedure. Specifically, the preparation process of NSBC and S/NSBC cathode is illustrated in Scheme 1.

Materials characterization

The morphologies and structures of the as-prepared samples were characterized using scanning electron microscopy (SEM, SU8020, Hitachi) and transmission electron microscopy (TEM, JEM-2100F, JEOL). The elemental distributions were investigated by energy dispersive spectrometry (EDS). The structural features were identified by X-ray diffraction (XRD, D/Max-2500V, Rigaku), Raman spectroscopy (LabRAM HR Evolution, Horiba) and X-ray photoelectron spectroscopy (XPS, ESCALAB 250Xi, Thermo Scientific). Thermogravimetric Analysis (TGA) was conducted on a thermal analysis instrument (Pyris 1 TGA, PerkinElmer, USA) at a heating rate of 10 °C min^{-1} in air. Nitrogen adsorption–desorption isotherms were measured using an automated surface area and porosity analyzer (Quadrasorb evo, Quantachrome, USA) for calculating the specific surface area (S_{BET}), total pore volume (TPV), and pore diameter distribution (PSD) based on the density functional theory (DFT).

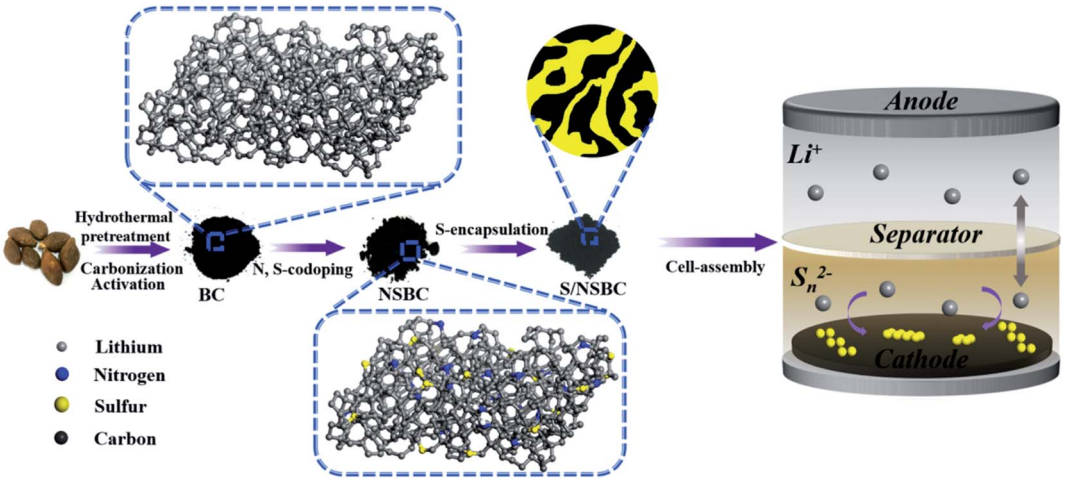

Scheme 1 Schematic for the preparation of BC, NSBC, S/NSBC and the assembled Li–S cells with S/NSBC cathode.

Cell assembly and electrochemical measurements

CR 2032 coin-cells with S/NSBC composite as the cathode, a Celgard 2500 membrane as the separator, and a Li foil as the anode were assembled in an Ar-filled glove box (see the cell structure, Scheme 1). A 1.0 M lithium bis(trifluoromethanesulfonyl)imide (LiTFSI) in 1,3-dioxolane (DOL) and 1,2-dimethoxyethane (DME) at 1 : 1 volume ratio with 1.0 wt% $LiNO_3$ additive was used as the electrolyte, and the electrolyte/sulfur ratio (E/S) of assembled coin cells was fixed to be 12 : 1 (μL mg^{-1}). Cyclic voltammograms (CVs) and electrochemical impedance spectroscopy (EIS) plots were collected on an electrochemical workstation (Autolab PGSTAT302N). Galvanostatic discharge/charge cycling tests were performed using a Land battery test system (Wuhan Land Electronic Co., China) within the voltage range of 1.7–2.8 V (*vs.* Li/Li^+). The specific capacities are calculated based on the sulfur mass and the theoretical capacity of sulfur (1675 mA g^{-1}).

Results and discussion

The NSBC powder was prepared *via* a two-step procedure of carbonization–activation combined with N, S-codoping by using hydrothermally treated BSS as the carbon precursor and thiourea as the heteroatom source. After the simultaneous carbonization–activation of carbon precursor, the as-prepared BC powder shows a 3D interconnected porous structure with quite smooth surface and an average size of several microns (Fig. S2a†), and only contains element C according to the EDS-mapping spectrum (Fig. S2b†). Compared to pristine BC, NSBC displays no distinct differences in structure and surface morphology (Fig. 1a and b), but contains trace amounts of N and S in addition to the element C (Fig. 1c–e matched with Fig. 1a), implying the effective doping of both element N and S. Both nitrogen and sulfur maps confirm the uniform distribution of doping element in the NSBC, and well match with carbon map. The typical HRTEM images (Fig. 1f and g) clearly show large number of micro–mesopores (white spots) within the NSBC, which is consistent with the type I adsorption–desorption isotherm collected for the NSBC (Fig. 2a). Massive micro–mesopores within the NSBC contribute a high S_{BET} of 2133.64 $m^2 g^{-1}$ with S_{micro} of 1920.55 $m^2 g^{-1}$. The TPV of NSBC reaches up to 1.076 $cm^3 g^{-1}$ with V_{micro} of 0.794 $cm^3 g^{-1}$, which allows the NSBC to have a theoretical sulfur loading of 66.2 wt% based on the density of liquid sulfur (1.82 g cm^{-3}).[35,42] PSD data of NSBC (Fig. 2b) show that the sharp peak locates at 1.76 nm, and most pores inside are less than 3 nm, confirming the characteristic micro–mesoporous structure of NSBC.

The structure and component of NSBC and BC were further determined by XRD, XPS and Raman spectroscopy. XRD patterns of both show a broad peak between 15 and 30°, indicating their characteristic of amorphous structure (Fig. 2c). Raman spectra of both show two prominent peaks located at 1350 and 1580 cm^{-1}, which correspond to the D and G band of carbon (Fig. 2d). The D band is attributed to the disordered sp^2 linked with sp^3 carbon or defective graphitic structure, and G band is assigned to the graphite-like sp^2 carbon.[34,43] The relative intensity of I_D/I_G indicates the disorder degree of carbon materials. The I_D/I_G values for BC and NSBC were calculated to be 0.97 and 1.10. The higher I_D/I_G for NSBC indicates that more defective structures were developed in NSBC induced by the introduction of substantial dopant atoms. In the XPS spectrum for NSBC (Fig. 3a), a C 1s peak (284.8 eV), an O 1s peak (533.3 eV), a N 1s peak (399.4 eV), and two S peaks (S 2p at 164.2 eV, S 2s at 227.2 eV) can be clearly discerned. As estimated by XPS data, the NSBC has a nitrogen doping level of 2.74% and sulfur doping level of 1.68%. In C 1s spectrum of the NSBC (Fig. 3b), four individual component peaks at 284.7, 286.0, 287.2, 289.3 eV are assigned to C–C/C=C, C–N/C–O/C–S, C=O and O–C=O,[44] respectively, demonstrating the successful codoping of N and S heteroatoms into the carbon framework. The N 1s spectrum of NSBC (Fig. 3c) can be divided into four fitted peaks at 398.8 eV, 400.2 eV, 401.7 eV, and 405.3 eV, corresponding to pyridinic N, pyrrolic N, quaternary N and oxidized N,[43,45] which are typically observed in N-doped carbon materials.

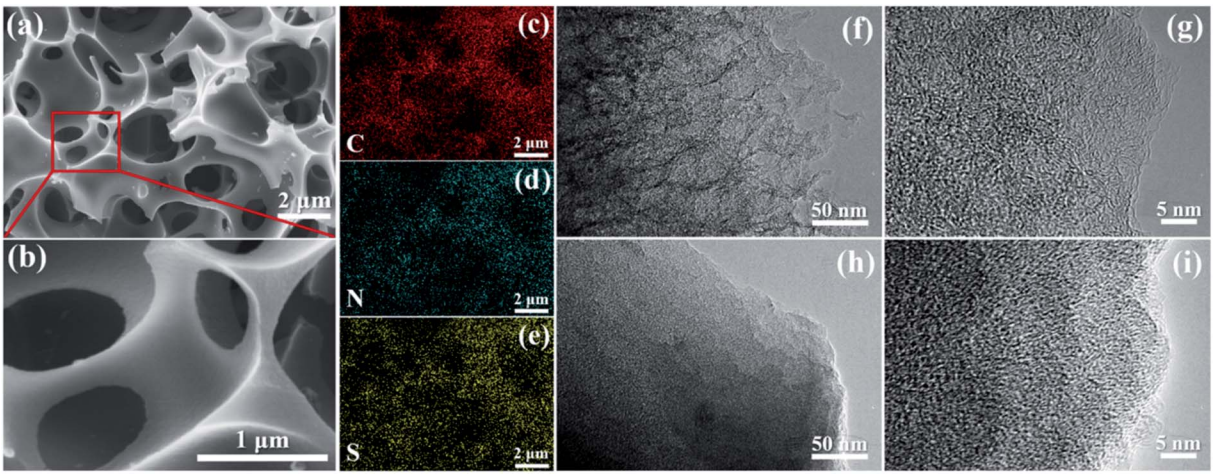

Fig. 1 Morphological and compositional characterizations for NSBC and S/NSBC: (a and b) SEM images of NSBC, (c–e) EDS mapping for the element C, N, and S, and HRTEM images for (f and g) NSBC and (h and i) S/NSBC.

Among them, the pyridinic N and pyrrolic N can generate strong chemical interaction with polar lithium polysulfides.[27–29] For the S 2p spectrum (Fig. 3d), S 2p can be deconvoluted into three peaks located at 163.9, 165.2, and 168.5 eV, which could be ascribed to S $2p_{3/2}$ and S $2p_{1/2}$ of sulfur groups (–C–S–C–), and oxidized sulfur species (–C–SO_x–C–).[44,46] The S-doped sites can increase the chemisorption of polysulfides with nonpolar carbon matrix through chemical binding of S_x^{2-}-doped S.[28,30] In order to visually examine and compare the polysulfide-trapping capability of NSBC and BC, a visual discrimination test was performed by dispersing NSBC or BC (20 mg) into the Li_2S_6 in DOL/DME solution (3 mM), and then comparing the solution color variation after aging for 12 h, as shown in Fig. 4.

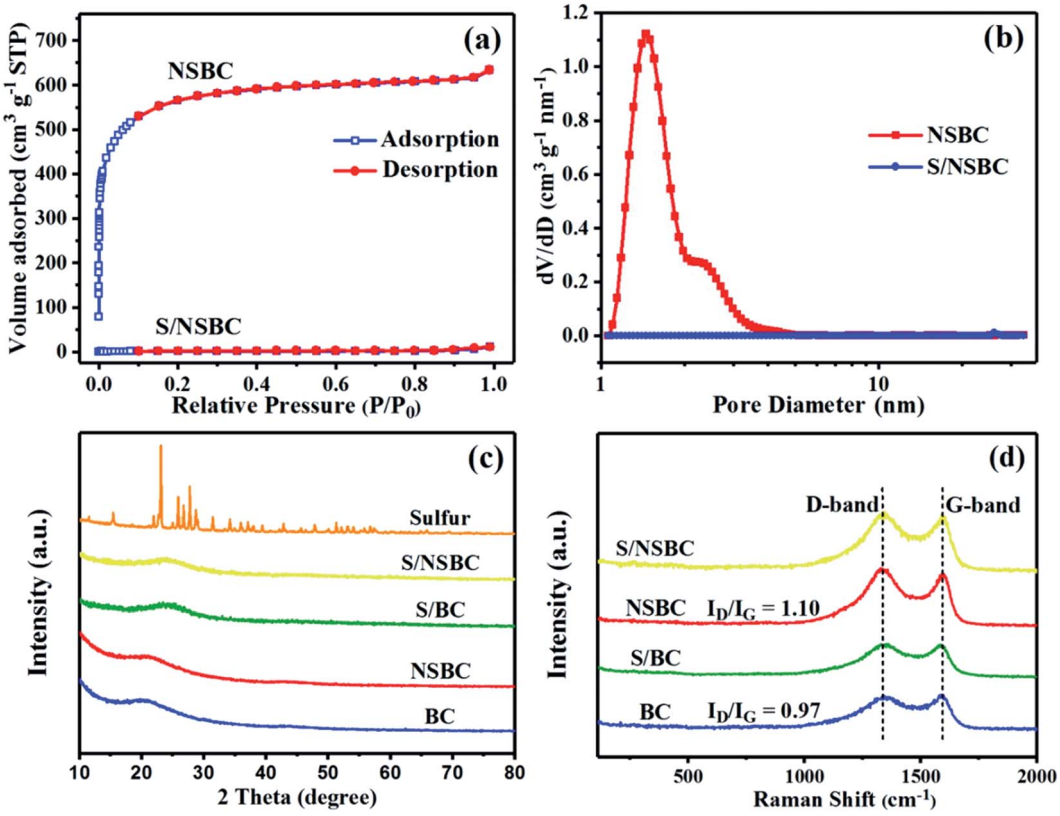

Fig. 2 Nitrogen adsorption–desorption isotherms (a), DFT pore size distribution (PSD) profiles (b) of NSBC and S/NSBC, and XRD patterns (c) and Raman spectrum (d) of NSBC, BC, S/NSBC and S/BC.

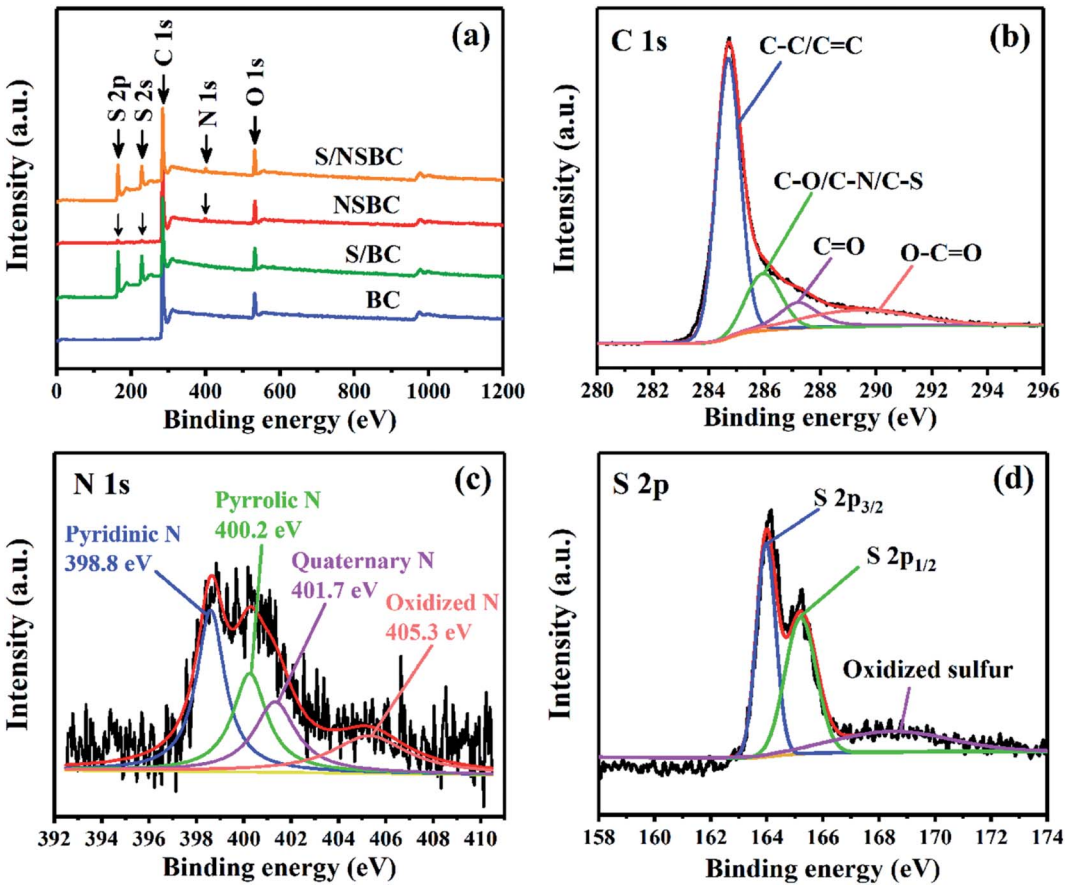

Fig. 3 XPS spectra of NSBC. Survey spectrum (a) and high-resolution spectra for C 1s, N 1s and S 2p (b–d).

Compared with the blank Li_2S_6 solution, the solution with BC changed from deep yellow to canary yellow. In contrast, the solution with NSBC became colorless transparent, demonstrating that introducing highly electronegative N and S atoms into carbon lattice indeed endows the NSBC with stronger affinity to absorb polysulfide species. Therefore, compare to BC, the NSBC is more capable of suppressing the diffusion of polysulfides and improving the utilization of sulfur. All characterization results of NSBC indicate that such 3D conductive frameworks with massive micro–mesopores and huge N, S-codoped polar surface should be competent enough to serve as a robust sulfur host.

The mechanism of interaction between NSBC and lithium polysulfides was further studied by density functional theory (DFT) calculation (see ESI† for computational methods). As shown in Fig. 5, the adsorption energies (E_{ad}) of S_8, Li_2S_8, Li_2S_6, Li_2S_4, Li_2S_2 and Li_2S on BC are −1.36 eV, −1.46 eV, −1.12 eV, −0.49 eV, −1.40 eV and −1.30 eV, respectively. Meanwhile, the E_{ad} of those on NSBC are −1.49 eV, −1.67 eV, −1.41 eV, −1.22 eV, −1.60 eV and −1.69 eV, respectively. The comparison shows that the latter series of data is higher than the former. The DFT calculation result reveals that the NSBC has stronger adsorption on lithium polysulfides. It is worth noting that, for the coordination of lithium polysulfide with the NSBC surface,

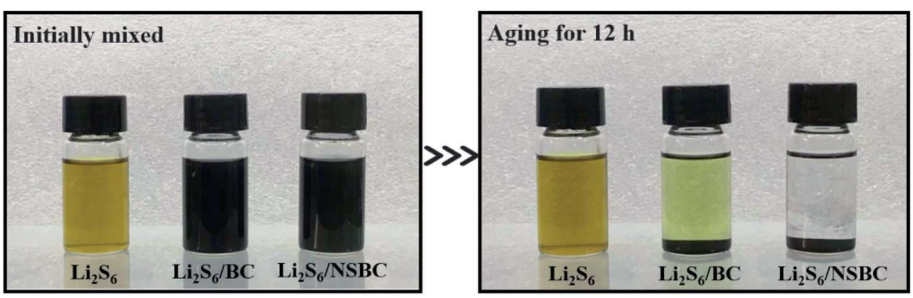

Fig. 4 Visual polysulfide adsorption test: digital images of Li_2S_6 in DOL/DME solution (3 mM) initially mixed with NSBC or BC powder (20 mg) and after aging for 12 h.

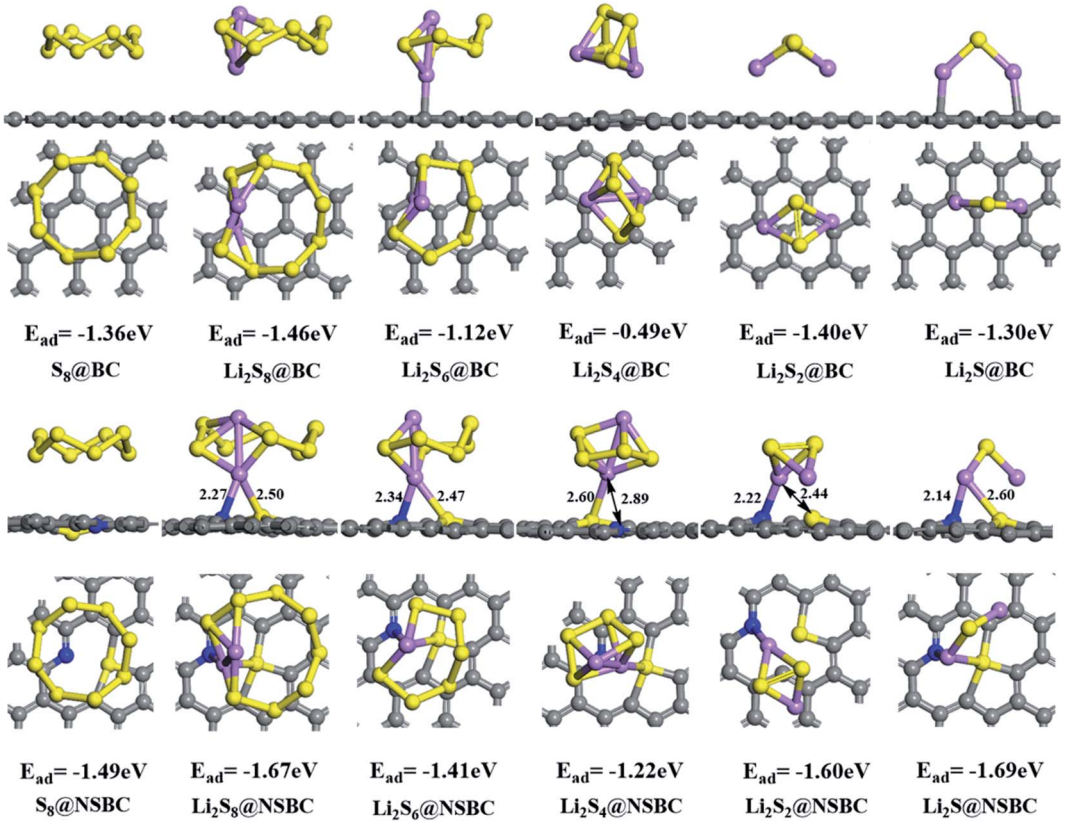

Fig. 5 The adsorption energies (E_{ad}) of S_8, Li_2S_8, Li_2S_6, Li_2S_4, Li_2S_2, Li_2S on BC and NSBC.

the interaction between Li and the N and S atoms coexists. Furthermore, XPS was performed to shed light on the interaction between NSBC and lithium polysulfides (the Li_2S_6 was selected as the model for lithium polysulfides). The Li_2S_6@NSBC for XPS analysis was obtained by filtrating the powder after the visual polysulfide adsorption test, and further dried under vacuum. The Li 1s spectrum of Li_2S_6@NSBC (Fig. S3b†) shows an additional peak at 56.2 eV with a +0.9 eV shift compared to the peak at 55.3 eV in the Li 1s spectrum of Li_2S_6 (Fig. S3a†), which can be assigned to Li–N bond.[47,48] In the S 2p spectrum of Li_2S_6 (Fig. S3c†), two fitted peaks located at 161.8 eV and 163.2 eV correspond to the terminal sulfur (S_T) and bridging sulfur (S_B),[49,50] respectively. In the S 2p spectrum of Li_2S_6@NSBC (Fig. S3d†), the S_B was not fitted since the binding energies of S_B overlaps with that of doped S, and the peak of S_T exhibits a +0.8 eV shift compared to the S_T in Li_2S_6, indicating a decrease in electron density on the S_T due to its interaction with doped sulfur in NSBC.[50] Meanwhile, the peaks at 166–172 eV could be ascribed to the S–O bonds.[51,52] Based on the above analysis, it could be concluded that the interaction between lithium polysulfides and N and S sites coexists.

Then, sulfur was infiltrated into the host matrix of NSBC *via* a melt-diffusion strategy. The obtained S/NSBC composite was firstly examined by SEM and TEM. The SEM images of S/NSBC (Fig. S5a and b†) show no evident difference in contrast with that of NSBC (Fig. 1a and b), indicating the successful encapsulation of sulfur within the inner pores of NSBC. The corresponding EDS mapping (Fig. S5c–e†) clearly corroborates that sulfur is homogeneously dispersed in the NSBC host matrix, and again confirms the effective nitrogen-doping of NSBC. Similar SEM result was also observed on S/BC composite (Fig. S6†), showing no obvious difference from that of BC, and confirming the effective sulfur infiltration as well. The HRTEM images of S/NSBC agree well with the SEM result that micro–mesopores (white spots) presented in the NSBC (Fig. 1f and g) almost disappeared in the S/NSBC (Fig. 1h and i). Besides, the color of S/NSBC becomes darker because of the sulfur infiltration into the pores of NSBC. Then, the S/NSBC and S/BC were further determined by XRD, TGA, nitrogen adsorption/desorption test and Raman spectroscopy. The characteristic diffraction peaks associated with the crystalline sulfur nearly disappeared in the patterns of both S/NSBC and S/BC (Fig. 2c), suggesting the effective encapsulation of sulfur into the micro–mesopores of carbon materials after sulfur infiltration. TGA plots (Fig. S7†) of S/NSBC delivers a mass loss of ~62 wt% from 200 to 500 °C, which is ascribed to the thermal evaporation of sulfur from S/NSBC. In addition, the TGA plot of S/NSBC shows a slightly lower evaporating speed and higher sulfur evaporating temperature than that of S/BC, which possibly dues to the interaction between the sulfur and the doped (N and S) atoms. S_{BET} and TPV of S/NSBC composite dramatically declined to 38.55 $m^2\ g^{-1}$ and 0.024 $cm^3\ g^{-1}$ (Fig. 2a), and all micro–mesopores in S/NSBC disappeared (Fig. 2b), revealing that inner pores have been filled up with sulfur. Raman peaks of sulfur did

not appear in the spectrum of S/NSBC and S/BC (Fig. 2d) due to the disturbance of the massive micro–mesopores on the Raman signals of the encapsulated sulfur.[53] All characterization results of S/NSBC manifest the effective infiltration of sulfur into the pores of the NSBC.

Li–S cells were assembled to evaluate the electrochemical performance of the S/NSBC composite as cathode materials (see the cell structure in Scheme 1). The CVs of the cells with S/NSBC cathode were collected at a scan rate of 0.1 mV s^{-1} within the voltage range of 1.7–2.8 V for the first five cycles, as shown in Fig. 6a. Two well-defined reduction peaks during the cathodic scans at around 2.3 and 2.0 V correspond to the stepwise reduction of sulfur (S_8) molecules to soluble long-chain polysulfides (S_n^{2-}, $4 \leq n \leq 8$), and further to insoluble short-chain polysulfides (Li_2S_2/Li_2S).[10,28] In addition, an extra broad and low reduction wave at 1.8 V appeared in the first cathodic scan because of the irreversible reduction of $LiNO_3$ in the electrolyte and the formation of protecting layer on the solid–electrolyte interface.[2,54] During the reverse anodic scans, there is only one oxidation peak centered at around 2.35 V, which corresponds to the reverse oxidation of Li_2S_2/Li_2S back to polysulfides and sulfur. The oxidation peak position remains stable at 2.35 V during the first five cycles, while two reduction peaks located at 2.27 and 2.01 V in the first scan are shifted to 2.30 and 2.04 eV in subsequent cycles, indicating a reduced polarization of the cell. With increase of cycle number, the CVs show no distinct change in terms of shape and peak position, indicating high electrochemical reversibility and stability of S/NSBC cathode. In addition, it could be found by comparing the CVs between S/NSBC and S/BC (Fig. 6a and b) that the CVs of S/NSBC present sharper and more intensive reduction and oxidation peaks, manifesting the enhancement of capacity and reaction kinetics of S/NSBC compared with S/BC electrode.

The GDC voltage profiles of S/NSBC at 0.1C, as shown in Fig. 6c, present two distinct discharge plateaus at around 2.30, 2.04 V and only one charge plateau at around 2.35 V, which correspond to the two reduction peaks and one oxidation peak in the CVs. Besides, it should be noticed that a slight plateau (the third discharge plateau) emerged at the terminal stage of the discharge process, which is ascribed to the deep reduction of low-order polysulfides (S_n^{2-}, $2 \leq n \leq 3$) to Li_2S,[55] contributing part of the theoretical capacity of sulfur electrode. Generally, such third discharge plateau could be detected in microporous C/S composite at a relatively low rate. Thus, the third discharge plateau presented in the GDC plot of S/NSBC confirm the abundance of micropores within the NSBC and deep reduction of polysulfides within the S/NSBC cathode. As a result, the initial discharge and charge capacities of S/NSBC electrode achieved 1478 and 1352 mA h g^{-1} respectively at 0.1C rate, with a coulombic efficiency (CE) of 91.5%. Such a high discharge capacity (close to 90% of the theoretical capacity of sulfur) indicates the deep lithiation of NSBC-confined sulfur in S/NSBC

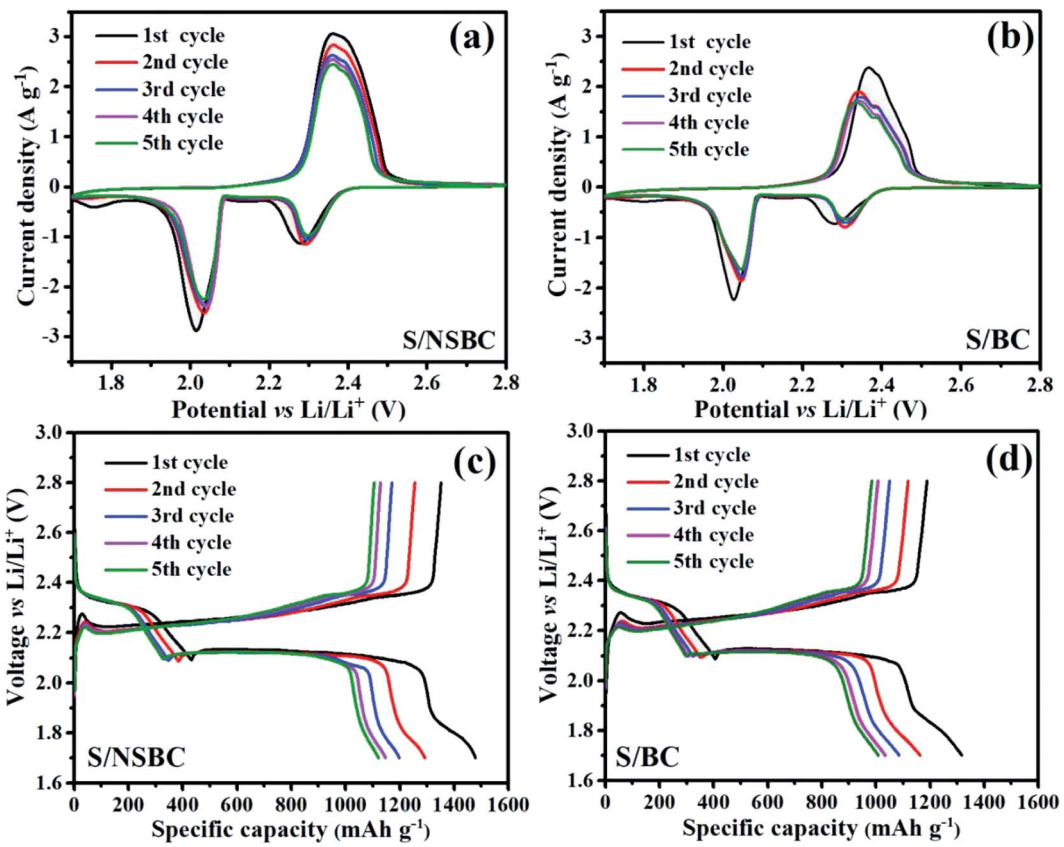

Fig. 6 (a and b) CVs of the initial five cycles at 0.1 mV s^{-1} and (c and d) voltage profiles of the initial five cycles at 0.1C for Li–S cells with the S/NSBC or S/BC cathode.

cathode.[35] As the cyclic discharge–charge proceeds, the insoluble products of Li_2S_2/Li_2S gradually block the carbon framework and decrease the efficiency of sulfur electrode, thus resulting in the weakening of the third discharge plateau. Moreover, it is clear that the capacity of S/NSBC is substantially higher than that of S/BC electrode at the same rate of 0.1C (Fig. 6c and d), and the voltage hysteresis (ΔE) of S/NSBC is smaller than that of S/BC cathode (179 *vs.* 207 mV, Fig. S8†), revealing the capacity enhancement and lower polarization of S/NSBC in comparison of S/BC electrode.

The long-term cycling stability of S/NSBC cathode was tested at 0.5C, as shown in Fig. 7a and S9a.† The initial specific discharge capacity was 1089 mA h g^{-1}, and decayed to 982 mA h g^{-1} after 3 cycles, representing a fast capacity decay (CD) of 9.84% during the initial several cycles, probably due to the solution loss of surface-adsorbed sulfur and dissolution of polysulfides from macropores into the electrolyte.[4,7] From the 4^{th} to 100^{th} cycles, the discharge capacity decreased from 982 to 730 mA h g^{-1} with CD of 25.6%, and then to 657 mA h g^{-1} at the 300^{th} cycle with extremely low CD of 6.4% for 200 cycles, and most notably and incredibly, the discharge capacities of S/NSBC cathode remain nearly constant from 300^{th} (657 mA h g^{-1}) to 500^{th} cycles (649 mA h g^{-1}), that is, the S/NSBC electrode basically achieves zero-capacity-decay for 200 cycles, which has rarely been reported in all published works associated with the biochar based S/C electrodes. Besides, the CE of the S/NSBC electrode remained close to 100% throughout the whole cycling process. In comparison, the cycling stability of S/BC cathode is obviously lower than that of S/NSBC cathode (Fig. 7a and S9†). The initial discharge capacity of S/BC cathode was 967 mA h g^{-1}, and then decayed continuously during the whole cycling. After 500 cycles, the S/BC cathode only retains a capacity of 359 mA h g^{-1}. Over the 500 cycles at 0.5C, the decay-rate of 0.08% per cycle for S/NSBC cathode is dramatically lower than that of S/BC cathode (0.126% per cycle). The superior cycling stability of S/NSBC to that of S/BC cathode could be attributed to the chemical interaction of lithium polysulfides with N and S sites, thereby suppressing the diffusion and shuttling of polysulfides and improving the utilization of sulfur. To further verify the application perspective of NSBC, the areal sulfur mass of S/NSBC cathode was increased to 2.8–3.0 mg cm^{-2}. As shown in Fig. S10,† the S/NSBC cathode still delivers a high initial specific capacity of 934 mA h g^{-1} at 0.5C, and still retained a stable discharge capacity of 526 mA h g^{-1} after 200 cycles, demonstrating the potential of NSBC for application.

The rate capability of S/NSBC cathode was also appraised by gradually increasing the charge–discharge current density from 0.1C to 2C every 10 cycles, as illustrated in Fig. 7b. The discharge capacities of S/NSBC electrode were 1464, 918, 793, 716, and 620 mA h g^{-1} at current densities of 0.1C, 0.2C, 0.5C, 1C, and 2C, respectively. When the rate is returned back to 0.1C, the discharge capacity can be recovered to ~950 mA h g^{-1}. The rate performance of S/BC cathode was examined as well (Fig. 7b). Even though the discharge–charge capacities of S/BC are lower than that of S/NSBC electrode at the same rate, it exhibited similar rate performance to that of S/NSBC. Such good

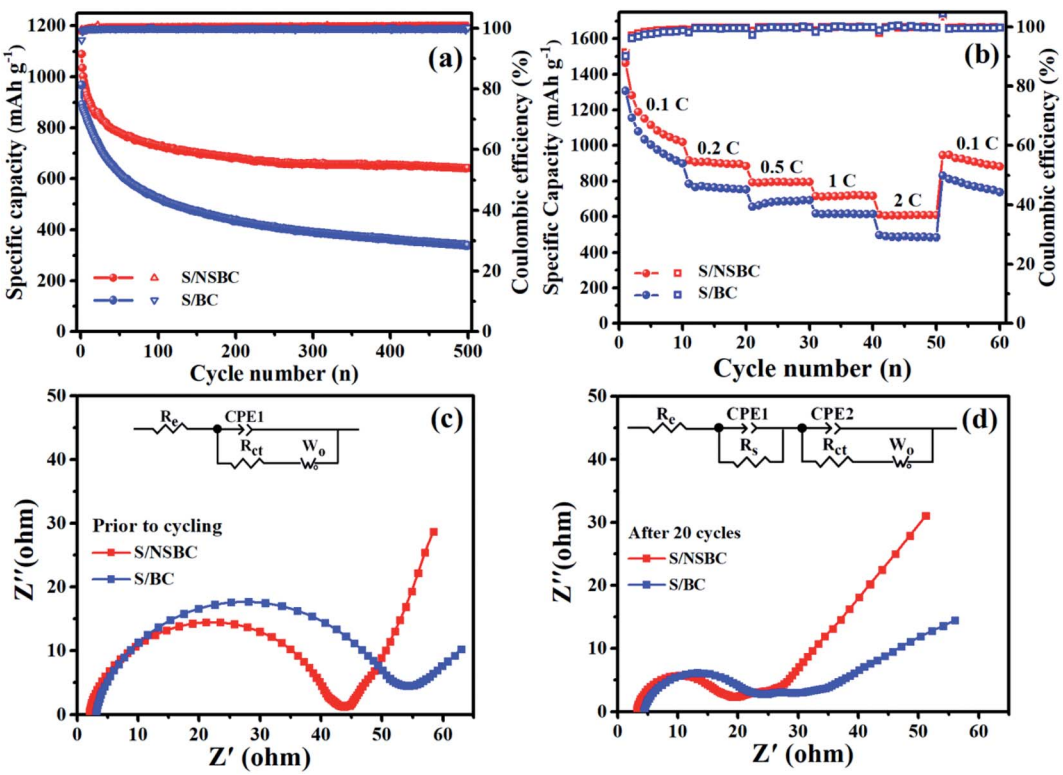

Fig. 7 (a) Cycling performance (at 0.5C), (b) rate performance at different current densities, and (c and d) EIS plots before and after cycling (at 0.5C) for Li–S cells with the S/NSBC or S/BC cathode (insets are the equivalent circuit models).

rate performances of S/C cathodes reveal the highly stable framework and good conductivity of the BSS-derived carbon matrix.

EIS measurements were carried out to further investigate the electrochemical kinetics process of both S/NSBC and S/BC electrodes before discharge and after 20 discharge–charge cycles at 0.5C in the frequency region from 100 mHz to 100 kHz. The EIS plots and the equivalent circuits used to fit the involved resistance values are presented in Fig. 7c and d, and the simulated values are listed in Table S1.† The plots of both S/NSBC and S/BC electrodes prior to discharge present a depressed semicircle at high frequency (HF) region attributed to the interface charge transfer resistances (R_{ct}) and a sloped line at low frequency (LF) region associated with the Li^+ diffusion at the electrode interface (Warburg impedance W_o).[6,56] The intercept at HF region on the real axis represents the electrolyte resistance (R_e), and obviously that the R_e in both cells are almost equal before cycling, and increased slightly after cycling due to the higher viscosity and lower ion mobility resulted from the polysulfides dissolution into the electrolyte, and the irreversible deposition of insulating Li_2S/Li_2S_2 onto the active surface of the electrode during cycling,[47] thereby leading to a slightly slower ion/electron transfer kinetics. Similarly, the W_o of both cells increased evidently after 20 cycles compare to that of the cells in before-discharge state, which is also because of the Li_2S_2/Li_2S layer deposition on the surface of the cathode.[56,57] Different from the plots collected before cycling, there are two depressed semicircles in the HF region of both plots measured at full charged state after 20 cycles. The former semicircle is attributed to the resistance (R_s) and capacitance (CPE1) on electrolyte/electrode interface resulting from the irreversible Li_2S_2/Li_2S layer deposition onto the electrode surface, and the latter semicircle mainly involves the charge transfer resistance (R_{ct}) and capacitance (CPE2). The R_{ct} of both cathodes decrease evidently after cycling, which could be attributed to the well activation of cathodes as well as the redistribution of active materials on the surface of cathodes.[58,59] Besides, the fitting results show that the overall impedances including R_{ct}, R_s, R_e and W_o of the cell with S/NSBC cathode are smaller than that of cell with S/BC cathode before and after cycling, demonstrating a faster Li^+ diffusion and charge transfer process, that is, an improvement of electrochemical kinetics within the S/NSBC cathode.

Additionally, the S/NSBC and S/BC cathodes in the initial state and after 50 cycles at 0.5C were characterized using SEM with EDS mapping to declare the strong confinement of active sulfur within NSBC. As can be seen by comparing that after discharge–charge cycling (Fig. 8), the electrode structure becomes condensed and rigid and maintains good integrity, and also no agglomeration of sulfur could be observed, manifesting the uniform passivation layer grown on the cathode surface. Besides, the sulfur contents in S/NSBC and S/BC were almost identical at initial state (Fig. S11 and Table S2†), while after cycling, the sulfur content for S/BC cathode declined to 38.2%, and the sulfur content of S/NSBC still maintained at 44.1%. The relatively lower sulfur loss in S/NSBC *versus* S/BC electrode during cycling demonstrates the stronger confinement of sulfur species within NSBC due to chemical interaction of N and S sites with polysulfides, thus enabling the S/NSBC cathode with higher utilization of sulfur, better cycling behavior and higher capacity retention.

Last, a comparison of the electrochemical performances of S/NSBC cathode with that of S/C cathodes based on different biomass-derived carbons[31–39,60–62] and other typical carbonaceous materials[63–65] was summarized in Table S3.† It is gratifying that the overall electrochemical performances S/NSBC

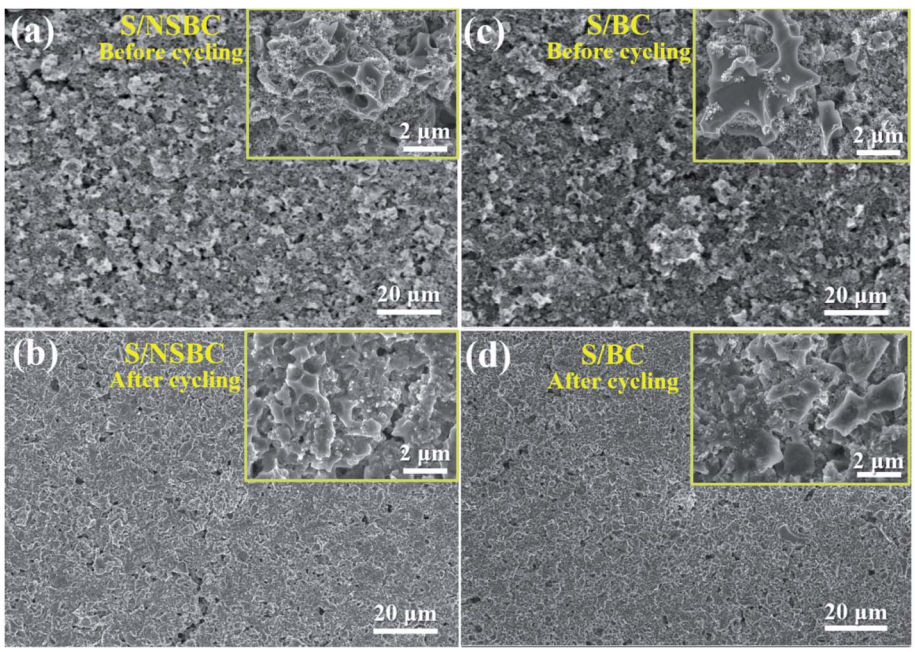

Fig. 8 Surface morphologies of S/NSBC (a and b) and S/BC (c and d) electrodes before cycling and after 50 cycles at 0.5C.

cathode developed in this work is comparable to the best performances reported. The superior electrochemical performance of S/NSBC could be attributed to the advantages in the unique structure and surface properties of the carbon substrate. Such 3D conductive frameworks of NSBC with massive micro–mesopores and huge N, S-codoped polar surface not only enable the homogenous sulfur distribution, improve the electrode–electrolyte contact as well as the sulfur–carbon contact, shorten the pathways for electron transport and ions diffusion, and physically confine the dissolved polysulfides within the pores, but also chemically anchor the polysulfides on the polar surface through chemical interaction between lithium polysulfides and N and S sites. In this way, the novel BSS-derived NSBC is competent enough to act as a distinguished sulfur host, and enables the S/NSBC cathode to show high discharge–charge capacity, good rate capability and long cycle stability.

Conclusions

In summary, a micro–mesoporous N, S-codoped carbon of NSBC derived from boat-fruited sterculia seed was synthesized and used as a sulfur host for Li–S batteries. After sulfur infiltration and cell assembly, the S/NSBC cathode shows outstanding discharge–charge performance, good rate capability, and especially ultrahigh cycle stability. A high initial discharge capacity of 1478 mA h g^{-1} was achieved at 0.1C, and the reversible discharge capacity was still remained at 649 mA h g^{-1} after 500 cycles at 0.5C with ultralow decay rate of 0.08% per cycle, and especially zero-capacity-decay after 300 cycles. Such superior electrochemical performance of S/NSBC cathode was enabled by the synergy of the unique 3D conductive micro–mesoporous frameworks and huge N, S-codoped polar surface within the NSBC. The combination of micro–mesoporous characteristics and N, S-codoping could physically confine the dissolved polysulfides within the pores, and chemically trap the polysulfides through chemical interaction of polysulfides with N and S sites. Therefore, the efficient utilization of sulfur, favorable reaction kinetics, and effective mitigation of polysulfide shuttling were achieved within the S/NSBC electrode. This work well confirms the great potential of utilizing the rich bioresources in energy storage materials and devices.

Conflicts of interest

There are no conflicts to declare.

Acknowledgements

The authors gratefully acknowledge the National Natural Science Foundation of China (51402078, 21702041, 11674354), 111 Project "New Materials and Technology for Clean Energy" (B18018), and the Fundamental Research Funds for the Central Universities (PA2017GDQT0023).

References

1 A. Manthiram, Y. Fu, S.-H. Chung, C. Zu and Y.-S. Su, Rechargeable lithium–sulfur batteries, *Chem. Rev.*, 2014, **114**(23), 11751–11787.
2 R. Fang, S. Zhao, Z. Sun, D. W. Wang, H. M. Cheng and F. Li, More Reliable Lithium-Sulfur Batteries: Status, Solutions and Prospects, *Adv. Mater.*, 2017, **29**(48), 1606823.
3 A. Rosenman, E. Markevich, G. Salitra, D. Aurbach, A. Garsuch and F. F. Chesneau, Review on Li-sulfur battery systems: an Integral perspective, *Adv. Energy Mater.*, 2015, **5**(16), 1500212.
4 Y. X. Yin, S. Xin, Y. G. Guo and L. J. Wan, Lithium–sulfur batteries: electrochemistry, materials, and prospects, *Angew. Chem., Int. Ed.*, 2013, **52**(50), 13186–13200.
5 Q. Pang, X. Liang, C. Y. Kwok and L. F. Nazar, Advances in lithium–sulfur batteries based on multifunctional cathodes and electrolytes, *Nat. Energy*, 2016, **1**(9), 16132.
6 S. Zhang, K. Ueno, K. Dokko and M. Watanabe, Recent advances in electrolytes for lithium–sulfur batteries, *Adv. Energy Mater.*, 2015, **5**(16), 1500117.
7 M. A. Pope and I. A. Aksay, Structural design of cathodes for Li-S batteries, *Adv. Energy Mater.*, 2015, **5**(16), 1500124.
8 R. Zhang, N. W. Li, X. B. Cheng, Y. X. Yin, Q. Zhang and Y. G. Guo, Advanced micro/nanostructures for lithium metal anodes, *Adv. Sci.*, 2017, **4**(3), 1600445.
9 J.-Q. Huang, Q. Zhang and F. Wei, Multi-functional separator/interlayer system for high-stable lithium-sulfur batteries: Progress and prospects, *Energy Storage Materials*, 2015, **1**, 127–145.
10 D.-W. Wang, Q. Zeng, G. Zhou, L. Yin, F. Li, H.-M. Cheng, I. R. Gentle and G. Q. M. Lu, Carbon–sulfur composites for Li–S batteries: status and prospects, *J. Mater. Chem. A*, 2013, **1**(33), 9382–9394.
11 G. Li, J. Sun, W. Hou, S. Jiang, Y. Huang and J. Geng, Three-dimensional porous carbon composites containing high sulfur nanoparticle content for high-performance lithium–sulfur batteries, *Nat. Commun.*, 2016, **7**, 10601.
12 J. Liang, Z.-H. Sun, F. Li and H.-M. Cheng, Carbon materials for Li–S batteries: functional evolution and performance improvement, *Energy Storage Materials*, 2016, **2**, 76–106.
13 Z. Li, Y. Jiang, L. Yuan, Z. Yi, C. Wu, Y. Liu, P. Strasser and Y. Huang, A highly ordered meso@ microporous carbon-supported sulfur@ smaller sulfur core–shell structured cathode for Li–S batteries, *ACS Nano*, 2014, **8**(9), 9295–9303.
14 L. Sun, D. Wang, Y. Luo, K. Wang, W. Kong, Y. Wu, L. Zhang, K. Jiang, Q. Li and Y. Zhang, Sulfur embedded in a mesoporous carbon nanotube network as a binder-free electrode for high-performance lithium–sulfur batteries, *ACS Nano*, 2015, **10**(1), 1300–1308.
15 F. Sun, J. Wang, H. Chen, W. Li, W. Qiao, D. Long and L. Ling, High efficiency immobilization of sulfur on nitrogen-enriched mesoporous carbons for Li–S batteries, *ACS Appl. Mater. Interfaces*, 2013, **5**(12), 5630–5638.
16 H. Wang, C. Zhang, Z. Chen, H. K. Liu and Z. Guo, Large-scale synthesis of ordered mesoporous carbon fiber and its

application as cathode material for lithium–sulfur batteries, *Carbon*, 2015, **81**, 782–787.

17 Z. Zhang, Z. Li, F. Hao, X. Wang, Q. Li, Y. Qi, R. Fan and L. Yin, 3D Interconnected Porous Carbon Aerogels as Sulfur Immobilizers for Sulfur Impregnation for Lithium-Sulfur Batteries with High Rate Capability and Cycling Stability, *Adv. Funct. Mater.*, 2014, **24**(17), 2500–2509.

18 Z. Li, X. Li, Y. Liao, X. Li and W. Li, Sulfur loaded in micropore-rich carbon aerogel as cathode of lithium-sulfur battery with improved cyclic stability, *J. Power Sources*, 2016, **334**, 23–30.

19 Y. Zhao, W. Wu, J. Li, Z. Xu and L. Guan, Encapsulating MWNTs into Hollow Porous Carbon Nanotubes: A Tube-in-Tube Carbon Nanostructure for High-Performance Lithium-Sulfur Batteries, *Adv. Mater.*, 2014, **26**(30), 5113–5118.

20 G. Zhou, D.-W. Wang, F. Li, P.-X. Hou, L. Yin, C. Liu, G. Q. M. Lu, I. R. Gentle and H.-M. Cheng, A flexible nanostructured sulphur–carbon nanotube cathode with high rate performance for Li-S batteries, *Energy Environ. Sci.*, 2012, **5**(10), 8901–8906.

21 L. Ma, H. L. Zhuang, S. Wei, K. E. Hendrickson, M. S. Kim, G. Cohn, R. G. Hennig and L. A. Archer, Enhanced Li–S batteries using amine-functionalized carbon nanotubes in the cathode, *ACS Nano*, 2015, **10**(1), 1050–1059.

22 R. Chen, T. Zhao, J. Lu, F. Wu, L. Li, J. Chen, G. Tan, Y. Ye and K. Amine, Graphene-based three-dimensional hierarchical sandwich-type architecture for high-performance Li/S batteries, *Nano Lett.*, 2013, **13**(10), 4642–4649.

23 C. Tang, Q. Zhang, M. Q. Zhao, J. Q. Huang, X. B. Cheng, G. L. Tian, H. J. Peng and F. Wei, Nitrogen-Doped Aligned Carbon Nanotube/Graphene Sandwiches: Facile Catalytic Growth on Bifunctional Natural Catalysts and Their Applications as Scaffolds for High-Rate Lithium-Sulfur Batteries, *Adv. Mater.*, 2014, **26**(35), 6100–6105.

24 L. Zhu, H.-J. Peng, J. Liang, J.-Q. Huang, C.-M. Chen, X. Guo, W. Zhu, P. Li and Q. Zhang, Interconnected carbon nanotube/graphene nanosphere scaffolds as free-standing paper electrode for high-rate and ultra-stable lithium–sulfur batteries, *Nano Energy*, 2015, **11**, 746–755.

25 X. Gu, C.-j. Tong, C. Lai, J. Qiu, X. Huang, W. Yang, B. Wen, L.-m. Liu, Y. Hou and S. Zhang, A porous nitrogen and phosphorous dual doped graphene blocking layer for high performance Li–S batteries, *J. Mater. Chem. A*, 2015, **3**(32), 16670–16678.

26 Q. Pang, X. Liang, C. Kwok and L. F. Nazar, The importance of chemical interactions between sulfur host materials and lithium polysulfides for advanced lithium-sulfur batteries, *J. Electrochem. Soc.*, 2015, **162**(14), A2567–A2576.

27 J. Song, T. Xu, M. L. Gordin, P. Zhu, D. Lv, Y. B. Jiang, Y. Chen, Y. Duan and D. Wang, Nitrogen-Doped Mesoporous Carbon Promoted Chemical Adsorption of Sulfur and Fabrication of High-Areal-Capacity Sulfur Cathode with Exceptional Cycling Stability for Lithium-Sulfur Batteries, *Adv. Funct. Mater.*, 2014, **24**(9), 1243–1250.

28 T. Z. Hou, X. Chen, H. J. Peng, J. Q. Huang, B. Q. Li, Q. Zhang and B. Li, Design Principles for Heteroatom-Doped Nanocarbon to Achieve Strong Anchoring of Polysulfides for Lithium–Sulfur Batteries, *Small*, 2016, **12**(24), 3283–3291.

29 J. Song, M. L. Gordin, T. Xu, S. Chen, Z. Yu, H. Sohn, J. Lu, Y. Ren, Y. Duan and D. Wang, Strong lithium polysulfide chemisorption on electroactive sites of nitrogen-doped carbon composites for high-performance lithium–sulfur battery cathodes, *Angew. Chem.*, 2015, **127**(14), 4399–4403.

30 G. Zhou, E. Paek, G. S. Hwang and A. Manthiram, Long-life Li/polysulphide batteries with high sulphur loading enabled by lightweight three-dimensional nitrogen/sulphur-codoped graphene sponge, *Nat. Commun.*, 2015, **6**, 7760.

31 J. Zhang, J. Xiang, Z. Dong, Y. Liu, Y. Wu, C. Xu and G. Du, Biomass derived activated carbon with 3D connected architecture for rechargeable lithium−sulfur batteries, *Electrochim. Acta*, 2014, **116**, 146–151.

32 Z. Sun, S. Wang, L. Yan, M. Xiao, D. Han and Y. Meng, Mesoporous carbon materials prepared from litchi shell as sulfur encapsulator for lithium-sulfur battery application, *J. Power Sources*, 2016, **324**, 547–555.

33 C. Hernández-Rentero, R. Córdoba, N. Moreno, A. Caballero, J. Morales, M. Olivares-Marín and V. Gómez-Serrano, Low-cost disordered carbons for Li/S batteries: A high-performance carbon with dual porosity derived from cherry pits, *Nano Res.*, 2018, **11**(1), 89–100.

34 J. Guo, J. Zhang, F. Jiang, S. Zhao, Q. Su and G. Du, Microporous carbon nanosheets derived from corncobs for lithium–sulfur batteries, *Electrochim. Acta*, 2015, **176**, 853–860.

35 Z.-H. Chen, X.-L. Du, J.-B. He, F. Li, Y. Wang, Y.-L. Li, B. Li and S. Xin, Porous coconut shell carbon offering high retention and deep lithiation of sulfur for lithium–sulfur batteries, *ACS Appl. Mater. Interfaces*, 2017, **9**(39), 33855–33862.

36 H. Wu, J. Mou, L. Zhou, Q. Zheng, N. Jiang and D. Lin, Cloud cap-like, hierarchically porous carbon derived from mushroom as an excellent host cathode for high performance lithium-sulfur batteries, *Electrochim. Acta*, 2016, **212**, 1021–1030.

37 M. Xiang, Y. Wang, J. Wu, Y. Guo, H. Wu, Y. Zhang and H. Liu, Natural silk cocoon derived nitrogen-doped porous carbon nanosheets for high performance lithium-sulfur batteries, *Electrochim. Acta*, 2017, **227**, 7–16.

38 M. K. Rybarczyk, H.-J. Peng, C. Tang, M. Lieder, Q. Zhang and M.-M. Titirici, Porous carbon derived from rice husks as sustainable bioresources: insights into the role of micro-/mesoporous hierarchy in hosting active species for lithium–sulphur batteries, *Green Chem.*, 2016, **18**(19), 5169–5179.

39 Y. Qu, Z. Zhang, X. Zhang, G. Ren, Y. Lai, Y. Liu and J. Li, Highly ordered nitrogen-rich mesoporous carbon derived from biomass waste for high-performance lithium–sulfur batteries, *Carbon*, 2015, **84**, 399–408.

40 O. D. Nartey and B. Zhao, Biochar preparation, characterization, and adsorptive capacity and its effect on

bioavailability of contaminants: an overview, *Adv. Mater. Sci. Eng.*, 2014, **2014**, 715398.

41 Y. Wu, S. W. Cui, J. Tang and X. Gu, Optimization of extraction process of crude polysaccharides from boat-fruited sterculia seeds by response surface methodology, *Food Chem.*, 2007, **105**(4), 1599–1605.

42 X. Ji, K. T. Lee and L. F. Nazar, A highly ordered nanostructured carbon–sulphur cathode for lithium–sulphur batteries, *Nat. Mater.*, 2009, **8**(6), 500.

43 C. Guizani, K. Haddad, L. Limousy and M. Jeguirim, New insights on the structural evolution of biomass char upon pyrolysis as revealed by the Raman spectroscopy and elemental analysis, *Carbon*, 2017, **119**, 519–521.

44 L. Miao, H. Duan, M. Liu, W. Lu, D. Zhu, T. Chen, L. Li and L. Gan, Poly (ionic liquid)-derived, N, S-codoped ultramicroporous carbon nanoparticles for supercapacitors, *Chem. Eng. J.*, 2017, **317**, 651–659.

45 K. Qu, Y. Zheng, S. Dai and S. Z. Qiao, Graphene oxide-polydopamine derived N, S-codoped carbon nanosheets as superior bifunctional electrocatalysts for oxygen reduction and evolution, *Nano Energy*, 2016, **19**, 373–381.

46 L. Qie, W. Chen, X. Xiong, C. Hu, F. Zou, P. Hu and Y. Huang, Sulfur-Doped Carbon with Enlarged Interlayer Distance as a High-Performance Anode Material for Sodium-Ion Batteries, *Adv. Sci.*, 2015, **2**(12), 1500195.

47 J. Xu, D.-W. Su, W.-X. Zhang, W.-Z. Bao and G.-X. Wang, A nitrogen-sulfur co-doped porous graphene matrix as a sulfur immobilizer for high performance lithium-sulfur batteries, *J. Mater. Chem. A*, 2016, **4**(44), 17381–17393.

48 D.-W. Su, M. Cortie and G.-X. Wang, Fabrication of N-doped Graphene-Carbon Nanotube Hybrids from Prussian Blue for Lithium-Sulfur Batteries, *Adv. Energy Mater.*, 2017, **7**(8), 1602014.

49 X. Chen, L.-X. Yuan, Z.-X. Hao, X.-X. Liu, J.-W. Xiang, Z.-R. Zhang, Y.-H. Huang and J. Xie, Free-Standing Mn3O4@CNF/S Paper Cathodes with High Sulfur Loading for Lithium-Sulfur Batteries, *ACS Appl. Mater. Interfaces*, 2018, **10**(16), 13406–13412.

50 Q. Pang, J.-T. Tang, H. Huang, X. Liang, C. Hart, K.-C. Tam and F. Nazar, Nitrogen and Sulfur Dual-Doped Carbon Derived from Polyrhodanine@Cellulose for Advanced Lithium-Sulfur Batteries, *Adv. Mater.*, 2015, **27**(39), 6021–6028.

51 W.-J. Xue, Q.-B. Yan, G.-Y. Xu, L.-M. Suo, Y.-M. Chen, C. Wang, C.-A. Wang and J. Li, Double-oxide sulfur host for advanced lithium-sulfur batteries, *Nano Energy*, 2017, **38**, 12–18.

52 J.-Q. Huang, Z.-L. Xu, S. Abouali, M. A. Garakani and K.-J. Kim, Porous graphene oxide/carbon nanotube hybrid films as interlayer for lithium-sulfur batteries, *Carbon*, 2016, **99**, 624–632.

53 X. Yang, L. Zhang, F. Zhang, Y. Huang and Y. Chen, Sulfur-infiltrated graphene-based layered porous carbon cathodes for high-performance lithium–sulfur batteries, *ACS Nano*, 2014, **8**(5), 5208–5215.

54 M. Barghamadi, A. S. Best, A. I. Bhatt, A. F. Hollenkamp, P. J. Mahon, M. Musameh and T. Rüther, Effect of LiNO3 additive and pyrrolidinium ionic liquid on the solid electrolyte interphase in the lithium–sulfur battery, *J. Power Sources*, 2015, **295**, 212–220.

55 V. Kolosnitsyn, E. Kuzmina and E. Karaseva, On the reasons for low sulphur utilization in the lithium–sulphur batteries, *J. Power Sources*, 2015, **274**, 203–210.

56 N. A. Canas, K. Hirose, B. Pascucci, N. Wagner, K. A. Friedrich and R. Hiesgen, Investigations of lithium–sulfur batteries using electrochemical impedance spectroscopy, *Electrochim. Acta*, 2013, **97**, 42–51.

57 B. Ding, Z. Chang, G. Xu, P. Nie, J. Wang, J. Pan, H. Dou and X. Zhang, Nanospace-confinement copolymerization strategy for encapsulating polymeric sulfur into porous carbon for lithium–sulfur batteries, *ACS Appl. Mater. Interfaces*, 2015, **7**(21), 11165–11171.

58 N.-P. Deng, J.-G. Ju, J. Yan, X.-H. Zhou, Q.-Q. Qin, K. Zhang, Y.-Y. Liang, Q.-X. Li, W.-M. Kang and B.-W. Cheng, CeF3-Doped Porous Carbon Nanofibers as Sulfur Immobilizers in Cathode Material for High-Performance Lithium-Sulfur Batteries, *ACS Appl. Mater. Interfaces*, 2018, **10**(15), 12626–12638.

59 B.-B. Zheng, N.-R. Li, J.-Y. Yang and J.-Y. Xi, Waste cotton cloth derived carbon microtube textile: a robust and scalable interlayer for lithium-sulfur batteries, *Chem. Commun.*, 2019, **55**(16), 2289–2292.

60 F. Schipper, A. Vizintin, J. Ren, R. Dominko and T. P. Fellinger, Biomass-Derived Heteroatom-Doped Carbon Aerogels from a Salt Melt Sol–Gel Synthesis and their Performance in Li–S Batteries, *ChemSusChem*, 2015, **8**(18), 3077–3083.

61 J. Zhang, Y. Cai, Q. Zhong, D. Lai and J. Yao, Porous nitrogen-doped carbon derived from silk fibroin protein encapsulating sulfur as a superior cathode material for high-performance lithium–sulfur batteries, *Nanoscale*, 2015, **7**(42), 17791–17797.

62 X. Li, X. Cheng, M. Gao, D. Ren, Y. Liu, Z. Guo, C. Shang, L. Sun and H. Pan, Amylose-Derived Macrohollow Core and Microporous Shell Carbon Spheres as Sulfur Host for Superior Lithium–Sulfur Battery Cathodes, *ACS Appl. Mater. Interfaces*, 2017, **9**(12), 10717–10729.

63 X. Li, Q. Sun, J. Liu, B. Xiao, R. Li and X. Sun, Tunable porous structure of metal organic framework derived carbon and the application in lithium–sulfur batteries, *J. Power Sources*, 2016, **302**, 174–179.

64 W. Ahn, M. H. Seo, Y.-S. Jun, D. U. Lee, F. M. Hassan, X. Wang, A. Yu and Z. Chen, Sulfur nanogranular film-coated three-dimensional graphene sponge-based high power lithium sulfur battery, *ACS Appl. Mater. Interfaces*, 2016, **8**(3), 1984–1991.

65 Z. Zhang, L. L. Kong, S. Liu, G. R. Li and X. P. Gao, A High-Efficiency Sulfur/Carbon Composite Based on 3D Graphene Nanosheet@ Carbon Nanotube Matrix as Cathode for Lithium–Sulfur Battery, *Adv. Energy Mater.*, 2017, **7**(11), 1602543.

